The Hot Main Kuiper Belt Size Distribution from OSSOS

Jean-Marc Petit[1] , Brett Gladman[2] , J. J. Kavelaars[2,3,4] , Michele T. Bannister[5] , Mike Alexandersen[6] ,
Kathryn Volk[7,8] , and Ying-Tung Chen[9]

[1] Institut UTINAM UMR6213, CNRS, OSU Theta F-25000 Besançon, France; Jean-Marc.Petit@normalesup.org
[2] Department of Physics and Astronomy, University of British Columbia, 6224 Agricultural Road, Vancouver, BC V6T 1Z1, Canada
[3] Herzberg Astronomy and Astrophysics Research Centre, National Research Council of Canada, 5071 West Saanich Road, Victoria, British Columbia V9E 2E7,
Canada
[4] Department of Physics and Astronomy, University of Victoria, Elliott Building, 3800 Finnerty Road, Victoria, BC V8P 5C2, Canada
[5] School of Physical and Chemical Sciences—Te Kura Matū, University of Canterbury, Private Bag 4800, Christchurch 8140, New Zealand
[6] Center for Astrophysics | Harvard & Smithsonian, 60 Garden Street, Cambridge, MA 02138, USA
[7] Lunar and Planetary Laboratory, The University of Arizona, 1629 E University Boulevard, Tucson, AZ 85721, USA
[8] Planetary Science Institute, 11700 East Fort Lowell, Suite 106, Tucson, AZ 85719, USA
[9] Institute of Astronomy and Astrophysics, Academia Sinica, No. 1, Section 4, Roosevelt Road, Taipei 10617, Taiwan
Received 2022 December 19; revised 2023 March 16; accepted 2023 March 16; published 2023 April 11

Abstract

Using the absolute detection calibration and abundant detections of the Outer Solar System Origins Survey project, we provide population measurements for the main Kuiper Belt. For absolute magnitude $H_r < 8.3$, there are 30,000 nonresonant main-belt objects, with twice as many hot-component objects than cold, and with total mass of 0.014 $M_\oplus$, only one-seventh of which is in the cold belt (assuming a cold-object albedo about half that of hot-component objects). We show that trans-Neptunian objects with $5.5 < H_r < 8.3$ (rough diameters 400–100 km) have indistinguishable absolute magnitude (size) distributions, regardless of being in the cold classical Kuiper Belt (thought to be primordial) or the "hot" population (believed to be implanted after having been formed elsewhere). We discuss how this result was not apparent in previous examinations of the size distribution due to the complications of fitting assumed power-law functional forms to the detections at differing depths. This shared size distribution is surprising in light of the common paradigm that the hot-population planetesimals formed in a higher density environment much closer to the Sun, in an environment that also (probably later) formed larger (dwarf planet and bigger) objects. If this paradigm is correct, our result implies that planetesimal formation was relatively insensitive to the local disk conditions and that the subsequent planet-building process in the hot population did not modify the shape of the planetesimal size distribution in this 50–300 km range.

Unified Astronomy Thesaurus concepts: Classical Kuiper belt objects (250); Luminosity function (942); Sky surveys (1464)

1. Introduction

The size distribution of objects produced at various stages of the planet formation process is a topic of intense interest (e.g., Kenyon 2002; Schaller & Brown 2007; Schlichting & Sari 2011; Kobayashi et al. 2016; Shannon et al. 2016; Ormel 2017). One must conceptually separate the size distribution of objects directly built by some planetesimal-formation process from those that are then created by either collisional grinding or accumulation (Kenyon et al. 2008; Morbidelli & Nesvorný 2020). In the main asteroid belt there has been heavy collisional modification that has greatly obscured the initial size distribution although arguments that many asteroids were "born big" have been made (Johansen et al. 2007; Morbidelli et al. 2009). The nonsaturated cratering record on Pluto/Charon and Arrokoth (Greenstreet et al. 2019; Singer et al. 2019; Spencer et al. 2020) argues that in the trans-Neptunian region, the size distribution has not been modified by collisional and accretional effects since the surfaces of these bodies formed. If true, this would mean that the currently essentially collisionless environment of the Kuiper Belt (Petit & Mousis 2004; Greenstreet et al. 2019; McKinnon et al. 2020; Abedin et al. 2021) has persisted for the solar system's age and

that the size distributions are thus primordial and preserve the outcome of the planetesimal-formation and planet-building process.

The recent study of Kavelaars et al. (2021) used an ensemble of survey samples (Kavelaars et al. 2009; Petit et al. 2011; Alexandersen et al. 2016; Petit et al. 2017; Bannister et al. 2018), referred to collectively as OSSOS++, to show that the dynamically cold classical Kuiper Belt's size distribution follows a power law with an exponential cutoff at the large-size end. This "exponential taper" shape is compatible with the initial mass function obtained in simulations of planetesimal formation in a streaming instability scenario (Schäfer et al. 2017; Li et al. 2019), and while other low-density formation scenarios exist (e.g., Shannon et al. 2016), which mechanism created planetesimals is irrelevant for this present manuscript. Several independent facts (Tegler et al. 2003; Petit & Mousis 2004; Parker & Kavelaars 2010; Pike et al. 2017; Greenstreet et al. 2019; Schwamb et al. 2019; McKinnon et al. 2020; Abedin et al. 2021) also hint at an in situ formation of the cold belt in a low-density environment.

The region where the cold belt resides, between the 3:2 and 2:1 mean motion resonance with Neptune, also contains resonant trans-Neptunian objects (TNOs) and other nonresonant, yet excited TNOs (objects with either large eccentricity e or inclination i or both) forming the hot belt. These objects are commonly stated to have been formed in a region closer to the Sun and then implanted in the Kuiper Belt during late planetary

migration, based on dynamical (reviewed by Nesvorný 2018) and compositional (Schwamb et al. 2019) arguments. The goal of this Letter is to use the OSSOS++ sample and compare the absolute magnitude distribution of the hot belt to that of the cold belt; we find that the two distributions are extremely similar over the magnitude range where we have high accuracy.

In Section 2, we present the OSSOS++ sample of hot objects and compare its size distribution to that of the cold population. We extend the OSSOS++ sample with the MPC database to the large-size side of the distribution. Next we present some cosmogonic implications of our findings.

2. The OSSOS++ Hot-population Absolute Magnitude Distribution

We use the OSSOS++ sample (see Bannister et al. 2018 for full details) to determine the absolute magnitude distribution of the populations of the main classical Kuiper Belt. The main-belt classicals are made up of the nonresonant, nonscattering objects with semimajor axes 39.4 au $< a <$ 47.7 au (that is, between the 3:2 and 2:1 resonances, rejecting all resonant objects in this range).

As explained in Van Laerhoven et al. (2019) and Kavelaars et al. (2021), the best single parameter to discriminate between the cold and the hot populations of the main classical Kuiper Belt is the free inclination with respect to the a-dependent Laplace plane. Huang et al. (2022a) provide an improved determination of the local Laplace plane by double-averaging over the two fast angles rather than from the classical first-order secular theory; the resulting free inclinations are very stable over time and can be found in Huang et al. (2022b).[10] Given the distribution of the free inclinations shown in Figure 3 of Huang et al. (2022a), in our Letter we elect to use $i_{free} < 4°.5$ as an acceptable split between the main-belt cold and hot populations (understanding there will be interlopers at some level). The *cold* classical belt only exists at $a >$ 42.4 au (Kavelaars et al. 2008) and is heavily concentrated to perihelia $q >$ 39 au (Petit et al. 2011; see also Figure 5 of Gladman & Volk 2021). We here adopt these simple cuts to define the cold classical-belt region, arguing that the higher eccentricities for TNOs with $q <$ 39 au and $a >$ 42.4 au indicate they have suffered dynamical excitation. The *hot* main-belt population is then all objects not in the cold sample. This yields 327 cold and 219 hot objects in OSSOS++.

2.1. Sample Characterization

We use the method in Kavelaars et al. (2021) to debias the orbit and H_r distributions of the OSSOS++ detections.[11] The most difficult TNO orbits to detect, at a given H_r, are those with near-circular orbits at the $a \simeq$ 47 au outer edge of the main belt. Objects on such orbits always remain at distance $d \simeq$ 47 au, while those with either lower a or larger eccentricity e will spend some time closer to the Sun and be visible for some fraction[12] of their orbital longitude. Because OSSOS++

---

[10] The main-belt free inclinations can also be found at http://yukunhuang.com.
[11] Divide the phase space in small (a, q, $\sin(i)$, H) cells; for any cell with a detection in it, determine the detection bias of this cell using the survey simulator.
[12] Using $H_r = 9.0$ as an example, $a = 47$ au circular orbits can never be observed by OSSOS, while $H_r = 9$ objects distributed along an $e \simeq 0.1$ orbit rise above the flux threshold close to perihelion and give one sensitivity to that set of a, q orbital elements for the purposes of debiasing (where debiasing is essentially taking into account Kepler's second law). The method has no ability, however, to debias the orbit for which there is never any possibility of detection.
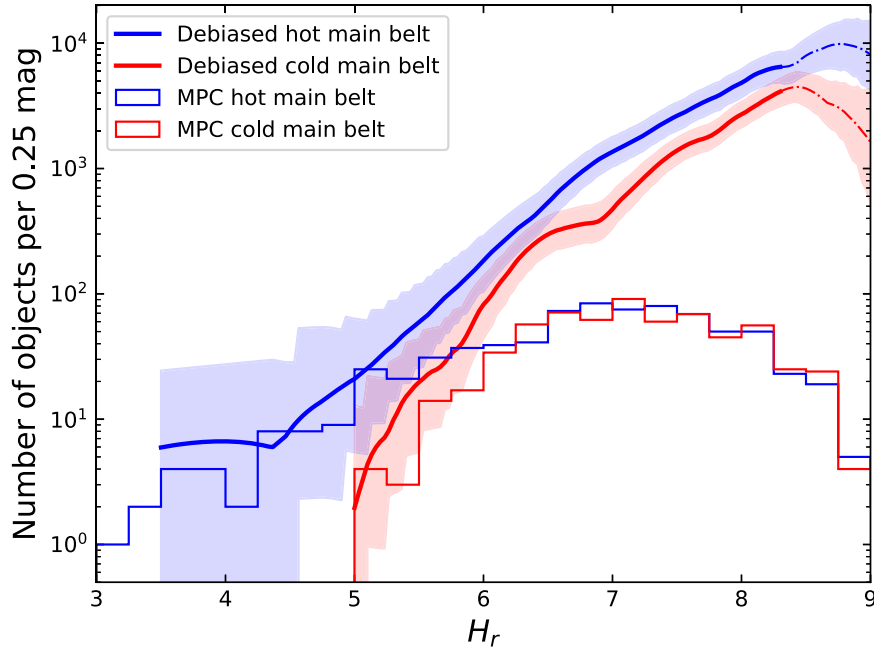
reached apparent magnitude $m_r \gtrsim 25$ for some blocks, $H_r \simeq 8.3$ TNOs are visible at 47 au; Kavelaars et al. (2021) used this H_r for the limit down to which we trust our debiasing for the cold population; even if the higher e of hot TNOs gives a mild increase in sensitivity to $H_r > 8.3$ hot-object orbits, we maintain the limit at 8.3 since our goal is to compare the two populations as a function of absolute magnitude. Because this debiasing method uses only the detections, this model will certainly increasingly underestimate TNO numbers beyond these sensitivity limits.

Simple binned histograms to represent a differential distribution are subject to large fluctuations when the sample is not very numerous. To avoid this shortcoming, we use a kernel density estimator (KDE) method that spreads out each detection over a kernel of some size; each detection thus contributes to the differential distribution not only at its exact position but on some interval with a varying weight (see Appendix A). Figure 1 presents these debiased differential TNO numbers (per 0.25 mag, in order to compare with the known sample in the Minor Planet Center, MPC) as the hot and cold populations implied by the OSSOS++ detections. MPC H magnitudes are converted to $H_r = H_{MPC} - 0.2$; this is the known shift between OSSOS++ H_r magnitudes and the H stated in the MPC. The rollover in the cold distribution for $H_r > 8.3$ where we expected insensitivity to begin is clear; the rollover in the hot distribution begins a few tenths of a magnitude fainter due to the ability to detect the lower perihelion objects present in that population (as mentioned in the above paragraph).

Several important results follow immediately from Figure 1. First, the MPC inventory (shown as histograms) of the main belt is very close to complete for $H_r < 5.3$; this was already clear for cold TNOs (Kavelaars et al. 2021), but our estimates reinforce the idea that the hot main-belt population is also now essentially complete. Sheppard et al. (2011) already suggested that the TNO inventory was nearly complete to apparent magnitude $M_R \simeq 21$, corresponding to $H_r \simeq 6.4$ at 30 au and $H_r \simeq 4.2$ at 50 au. Despite a burst of $H_r < 5.3$ discoveries during 2013–2015 by Pan-STARRS (Weryk et al. 2016), no bright main-belt TNOs have been discovered despite continued operations, signifying completeness to this magnitude. The agreement of our estimates with the complete population at the bright end shows that our debiasing method yields correct number estimates; these estimates then establish that $H_r > 5.8$ is largely incomplete (the known TNOs are below our 95% confidence intervals). The upcoming LSST will survey the main classical Kuiper Belt down to $H_r \simeq 7.5$ at 47 au; Figure 1 indicates that LSST will mostly discover TNOs at H magnitudes for which completeness in 2022 is still only $\simeq$5%. Second, one is struck that the hot and cold populations have rather similar H_r distribution shapes in the range [5.8, 8.3]. This is surprising because many papers (Bernstein et al. 2004; Elliot et al. 2005; Petit et al. 2011; Adams et al. 2014; Fraser et al. 2014) conclude that the hot and cold components have different absolute magnitude distributions. Here we suggest that these differences might be dominantly confined only to the largest ($H_r < 6$) TNOs of the populations; if true, this has major implications for planetesimal-formation and planet-building process.

Figure 1. Calibrated differential H_r distribution of the main-belt hot (blue bold curve) and cold (bold red curve) components from debiasing the OSSOS++ sample for $H_r \in [3; 8.3]$. Less secure estimates (see first and second paragraphs of Section 2.1) for $8.3 < H_r < 9$, which are only lower limits, are shown by dashed–dotted curves. These curves are Epanechnikov kernel density estimates (Appendix A) of the debiased H_r absolute magnitude distributions of the main classical-belt objects in OSSOS++. The colored areas represent 95% confidence intervals from Poisson statistics. Up to $H_r \simeq 5.3$, the OSSOS absolute calibration reproduces the MPC numbers, indicating the latter is now essentially complete in the main belt.

2.2. Comparison of the Hot and Cold Distributions

Figure 2 shows a clearer representation of the shape similarity of the two populations. Note that OSSOS++ has a sufficiently large number of detections so that construction of a differential H-magnitude and good resolution is possible; many past analyses have shown cumulative distributions. Here, we have multiplied the number of cold TNOs by a factor of 2.2, which matches the curves at $H_r = 6$. Given the uncertainties shown by the 95% confidence ranges and the expectation to have a small part of this range at $\simeq 2\sigma$ discrepancy, the shapes are nearly identical in the range from $5.5 < H_r < 8.3$, with the most compelling indication of a difference at $H_r < 6$ where the exponential taper cuts off the cold population. For $H_r < 5$, Figure 1 makes it clear that the hot population contains large objects, while the cold belt has none.

A χ^2 test can quantitatively evaluate if one can reject the null hypothesis that the two observed distributions are drawn from the same underlying distribution in the range from $\simeq 5.5$ to 8.3. In order to mitigate binning effects, we varied differential bin sizes (0.2, 0.3, or 0.4 mag) and the histogram starting magnitude (by steps of 0.1 mag), yielding probabilities that the two distributions are from the same underlying distribution ranging from 55% to 90%; the idea that the distributions are identical is clearly plausible. Figure 2 also shows the exponential taper function derived in Kavelaars et al. (2021); another χ^2 test to compare the hot H_r distribution to that function (only shifting the function to match the debiased hot number at the single value of $H_r = 8.0$) yields probabilities between 50% and 80% of drawing the hot population from the same functional form as the cold in this same H_r range.

Kavelaars et al. (2021) showed that if one extends the H_r-distribution beyond 8.3 with a functional form asymptotic to an exponential law $dN/dH \propto 10^{0.4H}$, the resulting estimated

differential numbers are consistent with the detection of three $H_r < 12$ cold TNOs in the Hubble Space Telescope (HST) search of Bernstein et al. (2004). A similar extrapolation of our hot main-belt population estimate is consistent with no hot detections in the HST search.[13] An asymptotic power of $0.4H_r$ is supported for $H_r \simeq 12$–17 by the crater record on Charon (Singer et al. 2019), which has been estimated to be dominated by hot-population projectiles (Greenstreet et al. 2015).

Thus, there is as yet no firm evidence that the shape of the H-magnitude distributions of the hot and cold are different for $H_r \gtrsim 5.5$. But if the cold classical belt is formed in situ in a low-density environment (exhibiting an exponential cutoff at a size scale set by local conditions at $\simeq 44$ au) and the hot object implanted after being formed much closer to the Sun (having a different formation, collision, and dynamical history), one might reasonably expect them to have very different H-magnitude distributions. We will return to this issue Section 5 after discussing the small-H regime, where the two populations differ markedly.

2.3. The Large-size Tail

The sample of large bodies from the main classical Kuiper Belt in the MPC database is very close to complete for the cold (Kavelaars et al. 2021; Figure 1) and the hot (Figure 1) populations down to $H_r \simeq 5.3$. Hence the H_r distribution at large sizes can be directly obtained from the MPC database. The debiased OSSOS++ sample fails to explore the $H_r < 4$ range due to limited sky area covered and the resulting tiny

---

[13] Despite the hot population having a factor of 2 more TNOs than the cold population at each $H_r > 5.8$ magnitude, nondetection in the HST survey is understood when one considers that these hot objects are spread out over 1 order of magnitude more sky area due to their larger orbital inclinations.
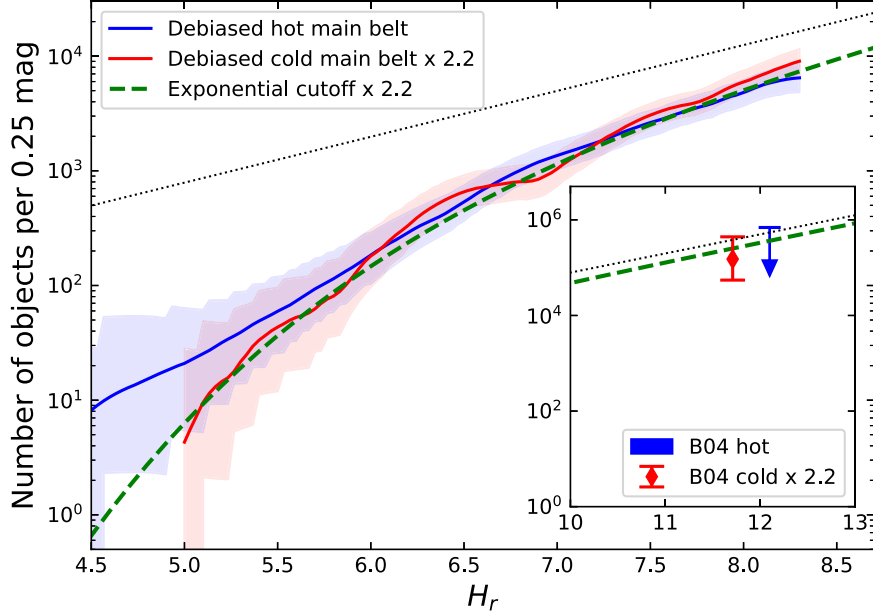
Figure 2. Similar to Figure 1, whereas here the debiased cold component estimates and uncertainties have been scaled upward by a factor of 2.2. The green dashed line shows the Kavelaars et al. (2021) cold-population exponential cutoff fit (with large-H asymptotic slope of 0.4), also scaled upward by a factor of 2.2. The inset shows the continuation of the scaled exponential cutoff fit at larger/fainter H_r; the red error bar gives the 95% confidence range from the detection of three cold TNOs using HST by Bernstein et al. (2004) and is compatible with the above extrapolation. The inset's blue arrow shows the 95% confidence upper limit from the nondetection of hot population TNOs in that same HST study. For $H_r > 5.5$ the shape of the hot and cold populations' curves are surprisingly similar, which hints at similar formation processes. The black dotted line is a reference exponential with logarithmic slope $\alpha = 0.4$ to help see how the exponential taper deviates from a single exponential.

number of detections (only one hot main-belt object brighter than $H_r = 5$ and three with $H_r < 5.5$).

Figure 3 shows the cumulative number of objects present in the MPC database for hot main classical belt (blue line) and all hot (black line) objects. It is noteworthy that the full hot sample, although obviously incomplete (because even the largest objects cannot be seen at the large distances reached by the scattering and resonant populations), is parallel to the hot main-belt sample, which is complete brightward of $H_r \simeq 5.3$. The abrupt change at $H_r \simeq 3.3$ in both distributions has been evident (Brown 2008) since large shallow surveys first covered most of the sky and continues to signal an abrupt change of exponential index between 0.14 and 0.6 at this magnitude (Ashton et al. 2021). We will refer to the $H_r < 3.3$ range as the "dwarf planet" regime[14] in the next paragraph and Section 5.

Fortuitously, the bright end of OSSOS++ happens to lie at the hot main-belt completeness limit. The argument above indicates we can graft our debiased hot distribution onto the MPC sample and, with the parallel distribution the full hot sample, allows one to have access to the H_r-magnitude distribution from Pluto/Eris scale down to $H_r = 8.3$ (and further by reasonable extension to the HST study's depth at $H \simeq 12$). The hot–cold comparison indicates that consistency of the H_r-magnitude shape for $H_r \gtrsim 5.5$ is not also true at bright absolute magnitudes. The cold population exhibits the exponential cutoff, while the hot population (both in the main belt and in general) not only lacks the exponential cutoff but has very shallow distribution as one goes up in size into the dwarf planet regime. We will interpret this in Section 5.

3. Consideration of Past Surveys

Because of the curved shape of the exponential cutoff, representing the H distribution by a single exponential $N(<H_r) \propto 10^{\alpha H_r}$ yields different logarithmic slopes α depending on the area and depth of the survey. A shallow, wide survey will probe the steep part of the curve, while a fainter, narrower survey will probe a shallower part of the curve. The case of the hot component is even worse due to the change between the logarithmic slopes of $\sim$0.6 in the range $H \in [3.5; 6]$ and 0.14 for brighter objects (Ashton et al. 2021). A single exponential representation will thus require a very shallow slope for wide, shallow surveys, to medium steep for intermediate surveys, and then again again shallow slopes for fainter surveys. Many of the early works did not separate between the hot and cold populations. Surveys close to the ecliptic were dominated by the cold component, while surveys mostly out of the ecliptic missed much or all of the cold population. To blur things even more, these studies used the apparent magnitude, thus convolving the H distribution with the distance distribution (see Petit et al. 2008 for a review).

More recent studies directly determined the H distribution, using either a single exponential when the range of H magnitudes is small (e.g., Petit et al. 2011; Adams et al. 2014) or a double exponential when the range of H magnitudes was large (Fraser et al. 2014). Petit et al. (2011) separately modeled the cold and hot components to their limit of $H_r \lesssim 7.5$ and obtained different size distributions for the two components, with population measurements to that H-magnitude limit. The number of $D > 100$ km TNOs in the hot and cold main belts given in Petit et al. (2011) were extrapolations with these single slopes (0.8 for hot and 1.2 for cold), beyond the range where they were measured. It is now clear that these slopes do not represent the H-magnitude distribution beyond 7.5 (which flattens steadily), and thus the extrapolation

---

[14] Although the current IAU dwarf planet definition involves difficult-to-know properties related to "roundness" (e.g., Tancredi & Favre 2008; Grundy et al. 2019), we point out that using a simple $H_V < 3.5$ definition would make the terminology adapt to some obvious transition in the object distribution.
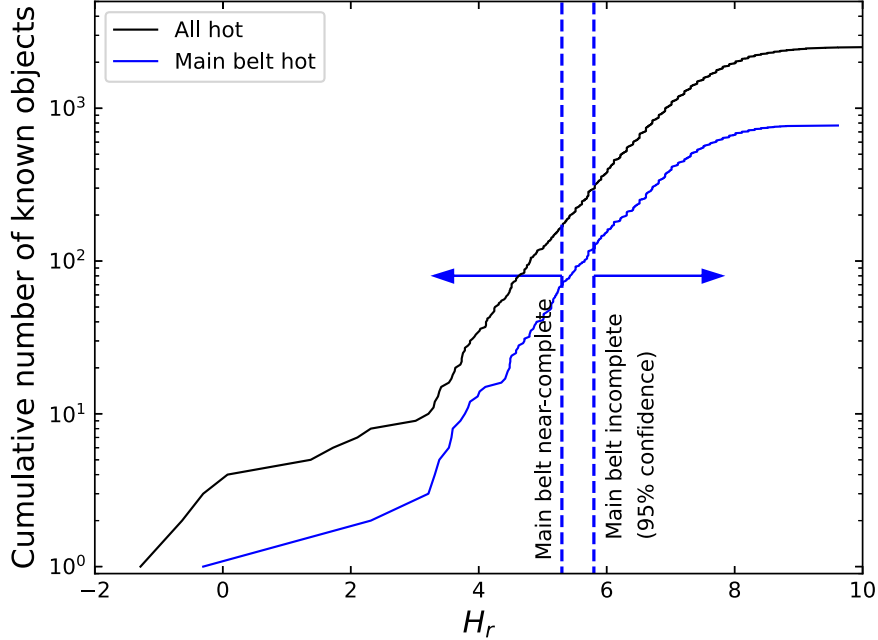
Figure 3. Cumulative H_r distribution (black curve) of all hot TNOs (here, $a > 29.5$ au and not in the cold population) in the MPC database as of 13 January 2022. The blue curve shows the main-belt subset. The vertical line at $H_r = 5.3$ represents where our analysis indicates that the the hot main-belt population is nearly complete. The vertical line at $H_r = 5.8$ shows where the MPC sample is certainly incomplete (95% confidence level). The two samples share very similar H_r distributions brighter than $H_r = 5.3$ (in particular, both distributions show an obviously shallower slope for $H_r < 3$), supporting the claim that all hot objects have the same origin.

Table 1
OSSOS++ Population Estimates from Direct Debiasing for Main-belt Nonresonant TNOs (in 10^3 Objects)

	$H_r \leqslant 8.3$	$D \geqslant 100$ km			
component		$\nu_r = 0.24$ ($H_r \leqslant 7.1$)	$\nu_r = 0.15$ ($H_r \leqslant 7.5$)	$\nu_r = 0.08$ ($H_r \leqslant 8.2$)	$\nu_r = 0.04$ ($H_r \leqslant 8.9$)
Cold	11 ± 1	1.2 ± 0.3	2.8 ± 0.5	9 ± 1	$^*20 \pm 2$
Hot	20 ± 3	2.4 ± 0.7	7 ± 1	18 ± 3	$^*46 \pm 7$
All	31 ± 4	3.6 ± 1	10 ± 2	27 ± 4	$^*66 \pm 9$

Note. Population estimates marked with a star are likely underestimates (Section 2.1) because $D = 100$ km corresponds to $H_r > 8.3$ for $\nu_r = 0.04$. The two left (right) columns in $D \geqslant 100$ km mostly cover the sample mean for the cold (hot) populations (respectively); although the literature gives different average albedos for the hot and cold populations, the uncertainty on individual measurements, possible systematics due to modeling, and the sample scatter means that individual object albedos could always cover the whole range, resulting in order of magnitude uncertainty in population estimates larger than D. In contrast, the $H_r < 8.3$ estimates are much more precise.

overestimated the $D > 100$ km populations , likely more so for the cold population than for the hot one. When including small (faint) TNO surveys, Fraser et al. (2014) used a double exponential with breaks around $H_r = 7$–8 where the bright part was essentially the same single exponentials for the two components as Petit et al. (2011).

The sparseness of data from homogeneous characterized surveys and the use of particular functional forms prevented the recognition of the similarity of the hot and cold size distributions in the few tens of kilometers to the ~ 300 km range.

4. Population and Mass Estimates

Using our derived H_r distribution, we can provide an accurate debiased main-belt population (which does not include resonant or scattering TNOs) as a function of H_r and also the number and mass estimates (which are more uncertain) for TNOs larger than a certain diameter.

4.1. Population Estimates

Table 1 gives estimated TNO numbers at the faintest absolute magnitude we confidently debias ($H_r \leqslant 8.3$) and for H_r values corresponding to a diameter $D = 100$ km for various commonly used values of the albedo (Equation (B2)). We added a column with $\nu_r = 0.24$, the albedo of Arrokoth determined by Hofgartner et al. (2021) in the r-band filter. Note that here all estimates are based on direct debiasing, which is very uncertain for $H_r = 8.9$. Alternately, to estimate numbers of $H_r < 8.9$ TNOs, one could use the exponential cutoff formula (Equation (B4)) for the cold population and multiply by 2.2 for the hot population; Table 1's last column would then read 21,000; 47,000; and 68,000 TNOs, which is identical given the uncertainties. This is consistent with our previous work at the older measurement limit: Petit et al. (2011) Table 5 estimated $N(H_g < 8.0) = (8 \pm 2) \times 10^3$, in agreement with our current $N(H_r < 7.3) = 6.7^{+1.3}_{-1.6} \times 10^3$ if one uses an averaged $g - r \simeq 0.7$ color.

Our debiasing gives an estimate of the total population of main-belt classical TNOs that we can compare to other well-sampled small-body populations. We note that the main classical Kuiper Belt contains 340 and 31,000 objects brighter than $H_r = 6.0$ and 8.3, respectively, while there are only 10 and 145 main-belt asteroids (MBAs) brighter than those magnitudes. Comparison with the Jovian Trojan population has more cosmogonic interest because the hot classicals and other excited TNOs have been suggested to come from the same primordial population as the Jovian Trojans (Morbidelli et al. 2005). In the $H_r = 7.3$–8.3 range, our debiasing shows that the Jovian Trojans have a similar H_r distribution to the hot TNO population, with the MPC Trojan sample being complete in that range (see Hendler & Malhotra 2020 for completeness limits). There are eight Jupiter Trojans with $H_r \leqslant 8.3$ and 20,000 hot main classical TNOs; thus, implantation models of Jovian Trojans and hot main classical TNOs must account for an efficiency ratio of order 3×10^3. Nesvorný & Vokrouhlický (2016) and Nesvorný et al. (2016) state implantation efficiencies of $(7 \pm 3) \times 10^{-4}$ and $(7.0 \pm 0.7) \times 10^{-7}$, respectively, for hot classicals and Jovian Trojans; this model-based factor of 1000 (with an uncertainty of at least a factor of 2) is thus similar to the observed factor of 3000. With OSSOS++, the $H_r < 8.3$ hot main-belt population is now the least fractionally uncertain number in this chain of reasoning but, as Table 1 shows, an order of magnitude population uncertainty appears due to the albedo uncertainty.

Using the CFEPS population estimates (Petit et al. 2011; Gladman et al. 2012) extrapolated to 100 km size, Greenstreet et al. (2015, 2019) and Abedin et al. (2021) determined the expected number of craters on the surface of Pluto, Charon, and Arrokoth formed in the last 4 Gyr of bombardment. They extrapolated the 100 km population down to kilometer-size projectiles using an exponential of slope $\alpha = 0.4$, concluding that the recorded crater numbers could be produced without a contribution of an early phase (see Section 5) and that the dominant source of craters on Arrokoth is from cold-population projectiles.

Our current estimates, however, indicate fewer 100 km bodies than the CFEPS extrapolation down to this size, by a factor of 3–30 depending on which albedo is used (which determines H for 100 km bodies.)[15] Starting from $H \sim 6$ down to the limit of our survey, we find that the hot population is 2.2 times larger than the cold. For smaller sizes (larger H), we *assume* that the exponential cutoff continues; thus, the hot population remains twice the cold at any given H_r. Equation (B4) then yields similar numbers of projectiles at $H_r \sim 17$ as found by Greenstreet et al. (2015, 2019) and Abedin et al. (2021), with now twice as many main-belt hot TNOs as cold, while before, the extrapolation produced 2–3 times as many cold objects as hot due to the incorrect continuation of a very steep slope for cold objects to $H_g = 8$. The ratio of hot-to-cold could be even larger at a specific size (km) when one accounts for the possibly larger albedo for cold objects ($\nu_r \sim 0.15$) than for hot objects ($\nu_r \sim 0.08$). Remember that all this is an assumption, not directly based on observational evidence, and should be taken with a pinch of salt.

Thus all other astronomers who worked on the crater counts on Arrokoth, Pluto, and Charon should now reevaluate the Arrokoth cratering rate. Pluto and Charon will continue to be dominated by hot-population projectiles, while Arrokoth may cease to be dominated by cold-population impactors. Morbidelli et al. (2021) concluded dominance of the hot population for Arrokoth crater formation, but their numbers of 100 km and 2 km projectiles are not in line with our current estimates and should be revisited.

4.2. Mass Estimates

In Appendix B, we estimate the main-belt mass between the 3:2 and 2:1 mean-motion resonances, integrated over *all* sizes. We use bulk density $\rho = 1000$ kg m^{-3} and albedos $\nu_{r,c} = 0.15$ and $\nu_{r,h} = 0.08$ for cold and hot TNOs, respectively (Fraser et al. 2014; Lacerda et al. 2014),[16] except for objects larger than ~ 500 km, where both density and albedo are known to increase (see Appendices B.1 and B.2).

Understanding that masses are uncertain to a factor of 3 due to poorly constrained albedos and densities, we find a cold-belt mass of $0.002\, M_\oplus$ for an exponential cutoff shape of H_r and $0.012\, M_\oplus$ for the hot belt, for a total mass of the main classical belt of $0.014\, M_\oplus$. We find the same hot-belt mass as Fraser et al. (2014), but a cold-belt mass that is 7 times larger. Gladman et al. (2001) estimated a total mass for the 30–50 au distance range of 0.04–0.1 $M_\oplus$, using an albedo $\nu_r = 0.04$ for all TNOs; this includes all dynamical components, but because the main belt represents only about half the mass (determined using the CFEPS model; Petit et al. 2011) in the 30–50 au distance range, a 0.02–0.05 $M_\oplus$ estimate results. Using this 4% albedo, our current approach gives a slightly higher total classical main-belt mass $0.06\, M_\oplus$.

Based on creation of a planetary ephemeris, Di Ruscio et al. (2020) estimated the total Kuiper Belt mass to be $(0.061 \pm 0.001)M_\oplus$, with unknown model-based uncertainty. This is $\simeq 4$ times higher than our estimate of the classical belt, but again only half of this $0.06M_\oplus$ would be main-belt TNOs. With the same method but using a slightly different data set, Pitjeva & Pitjev (2018) estimated the mass to be $(0.02 \pm 0.004)M_\oplus$, which when restricted to the main belt is in agreement with our estimate.

Because the tapered exponential lacks an abrupt break between a steep slope power law (steeper than $\alpha = 0.6$ for H_r distribution or than $q = 4$ for D distribution[17]) and a shallow slope for small sizes, there is less of a concentration of mass in the typical diameter scale where the break occurs. For our estimated hot belt, the 25th and 75th percentiles for mass are $H_r < 6.7$ and $H_r < 9.8$. For the cold population, the 25th percentile is $H_r < 7.3$, and the 75th percentile is at $H_r < 10.1$. Broadly speaking, our precise knowledge of the size distribution includes an H-magnitude range that contains about half the mass of the classical Kuiper Belt.

Note that because of the very shallow $\alpha = 0.14$ (Ashton et al. 2021) in the $H_r < 3.5$ hot-object tail, it is possible that the largest TNOs in this tail were of planetary scale and contained most of the mass of the hot-population formation region. These very massive objects have not been retained the hot main-belt or the hot population in general due to the $\sim 10^{-3}$ retention

---

[15] Petit et al. (2011) used an albedo $\nu_g = 0.05$, which means $\nu_r \sim 0.08$ for cold objects (assuming $\langle g - r \rangle \sim 0.9$) and $\nu_r \sim 0.06$ for hot objects (for $\langle g - r \rangle \sim 0.6$). If one instead uses $\nu_r = 0.15$ for cold and $\nu_r = 0.08$ for hot (see Appendix B), this means a brighter H_r magnitude for 100 km, again decreasing the number of objects at that size.

[16] Note that Vilenius et al. (2014) reported very similar values of $\nu_{v,c} \sim 0.14$ and $\nu_{v,h} \sim 0.085$ in band v from Herschel and Spitzer observations.

[17] The relations $N(<H) \propto 10^{\alpha H}$ and $dN/dD(D) = n(D) \propto D^{-q}$ are related by $q = 5\alpha + 1$ for a fixed albedo ν.

efficiency of the scattering-out process (Nesvorný & Vokrouhlický 2016), and thus, one should remember that much of mass in the hot-formation region may have been sequestered into very large (now absent) planetary-scale objects.

5. Discussion of Cosmogonic Implications

Based on several lines of evidence (see Kavelaars et al. 2021 and reference therein), the cold population is primordial, meaning its H_r distribution has not evolved since the formation epoch. Given the shape similarity of the hot and cold populations in the range $H_r \simeq 5.5$–8.3, we hypothesize that the hot population has also preserved its primordial shape in that size range, and the same physical mechanism was responsible for the accretion of bodies of that size in both the hot- and cold-forming regions. The physical conditions (e.g., temperature, dynamical timescales) were likely very different in these two regions, and in particular the surface density in solids would likely have been orders of magnitude larger in the hot-forming region than at $\simeq 43$ au (Gomes et al. 2004; Nesvorný et al. 2020). If true, it follows that the formed planetesimal size distribution is at most a weak function of the local conditions, at least in the $H_r = 5.5$–8.3 range; over this range it is steeper than collisional equilibrium. Coupled with the match to the cold (believed to be primordial and unevolved) population, we thus conclude that at this size scale there was no appreciable collisional modification of the shape. This implies that the initial phase during which the hot population was in a dense collisional environment was of shorter duration than the collisional lifetime of $D \simeq 100$ km bodies. Benavidez et al. (2022) supports this picture, showing that the $D \gtrsim 100$ km size distribution's shape does not change. They also conclude that long (100 Myr) instability phases do not produce successful matches to observational constraints.

Nesvorný et al. (2020) and Kavelaars et al. (2021) suggested that a candidate for this initial planetesimal forming phase is the gravitational/streaming instability (GI/SI). The numerical simulations typically yield a size distribution that can be fit with an exponential cutoff functional form (Abod et al. 2019) that is also a good match to the cold population. Here we have shown that it is also a good match to the hot population with $D \lesssim 300$ km.

Our paradigm is that after planetesimal formation, the conditions in the hot-population formation region (in particular, much higher surface density) permitted the creation of bigger objects, which thus erased the taper for $H_r < 5.5$. An important implication is that dwarf planets and larger objects then accumulated mass without altering the relative size distribution in the $H_r \simeq 6$–9 range (and possibly much smaller sizes). Two main mechanisms are usually invoked for this latter stage of accretion: runaway growth (reviewed by Lissauer 1993) and pebble accretion (e.g., Ormel 2017). Runaway growth does not care about the size of objects it sweeps up, while in pebble accretion the very big object mass accretion is from tiny pebbles. In this later case, our result implies that objects with sizes corresponding to $H_r = 5.5$–8.3 accumulate negligible further mass via pebbles.

If GI/SI is the planetesimal-formation mechanism, scalings indicate that the mass of the largest bodies formed is governed by the local solid surface density (to the third power) and heliocentric distance (to the sixth power) (Abod et al. 2019; Li et al. 2019). For a surface density varying with heliocentric distance to the -1.5 or -2 power between 25 and 45 au, this would not be a problem as the density drop would roughly compensate for the increase in distance. However, there are

arguments that the surface density drops by a factor of ~ 1000 between these locations (i.e., Nesvorný et al. 2020). It is thus surprising that two populations would have the same exponential cutoff shape. Some possible solutions to this dilemma are

1. the initial planetesimal-formation process is actually only mildly sensitive to the density, but the creation of $H_r < 5$ bodies in the hot-population formation region proceeded efficiently, while in the cold belt these dynamics were not triggered due to the low surface density, or
2. cold-population formation occurred in a localized over-density (perhaps caused by a pressure bump) in an environment where the formed planetesimals are not confined to the overdense region, while in contrast, the hot population formed in an extended high-density zone where large-object formation was possible through another process.

The first possibility is supported by Klahr & Schreiber (2020), who derive a criterion for the *minimum* object mass that can be created by GI/SI when accounting for diffusion due to turbulence. Based on this criterion, they claim that the size distribution should be Gaussian centered on this minimum size ($D \simeq 80$–85 km with width ~ 45 km). Their minimum size is fairly insensitive to heliocentric distance from 3 to 30 au but then drops markedly at larger distances.

The second possibility would have to be the solution if GI/SI is the dominant mechanism, unless the current theoretical scaling laws are incorrect. In these studies, there is a trigger density one gets to, and then GI/SI forms planetesimals quickly. This could result in the two regions having the same shape because they both reached the same critical density although the way they achieved that density would have been different between the two populations.

Summarizing our discussion, we hypothesize that whatever mechanism created the first planetesimals up to ~ 400 km in diameter, it is largely insensitive to the global physical conditions and produces objects up to that size. In dense environments, some other process(es) takes over to build bigger objects, without altering the size distribution from ~ 300 km down to a few tens of kilometers or even less.

Appendix A
Kernel Density Estimator (KDE)

To avoid the shortcomings of classical histograms due to size and location of the bins, we use a kernel density estimator (KDE; Rosenblatt 1956; Parzen 1962) to estimate the true H_r distribution.[18] The kernel is a nonnegative function that smooths the contribution of each datum over an interval whose size is determined by the *bandwidth* parameter. There exists a variety of kernels; we use an Epanechnikov finite extent kernel (Epanechnikov 1969), as it is optimal in a mean square error sense.

The bandwidth is an important parameter that we determine using the empirical approach of cross-validation. This empirical approach to model parameter selection does not depend on (dubious) assumptions about the underlying data's distribution and thus is very flexible. For the cold OSSOS++ sample, the optimal bandwidth is 0.4, which we use to plot Figure 1. For the hot sample, the optimal bandwidth depends rather strongly on the inclusion or exclusion of the few objects at the tails of the distribution, especially at the bright end where the H_r spread is very uneven. This means that the best bandwidth is very different at the large-size and the small-size ends of the range, so we renormalize the H_r values to make them more uniform ($Y_r = 10^{0.1(H_r-9)}$) and then use an optimal bandwidth of 0.1 in this new variable.

In our computations, we use the implementation from the scikit-learn Python package (Pedregosa et al. 2011). We then scale the KDE to the total number of objects in each component of the main classical Kuiper Belt per magnitude and show the result in Figure 1.

Appendix B
Mass of the Belt

We first derive the relation between H_r and the TNO mass M. The apparent magnitude m_r in a given filter band (CFHTLS-r' here) is related to its radius r, in kilometers; its geometric albedo ν_r; its distance to the Sun R and to the observer on Earth Δ (both in astronomical units); its phase angle γ; the phase function $\Phi(\gamma)$; the rotational lightcurve function $f(t)$; and the magnitude of the Sun $m_{r,\mathrm{Sun}}$ in the same band by

$$m_r = m_{r,\mathrm{Sun}} - 2.5\log_{10}\left(\nu_r\left(\frac{r}{1\,\mathrm{km}}\right)^2\Phi(\gamma)f(t)\right)$$
$$+ 2.5\log_{10}\left(2.25 \times 10^{16}\frac{R^2\Delta^2}{\mathrm{au}^4}\right). \quad (B1)$$

Here we assume $f(t) = 1$ as the average of a rapid periodic function. From H_r definition, we have

$$H_r = m_r + 2.5\log_{10}(\Phi(\gamma)) - 2.5\log_{10}\left(\frac{R^2\Delta^2}{\mathrm{au}^4}\right)$$
$$= m_{r,\mathrm{Sun}} + 2.5\log_{10}(2.25 \times 10^{16})$$
$$- 2.5\log_{10}\left(\nu_r\left(\frac{r}{1\,\mathrm{km}}\right)^2\right).$$

---

[18] See https://en.wikipedia.org/wiki/Kernel_density_estimation for an easy and basic introduction to KDEs.

For the cfhtls-r filter, $m_{r,\mathrm{Sun}} = -26.94$ in the AB system (Willmer 2008), and therefore

$$H_r = 13.94 - 2.5\log_{10}\left(\nu_r\left(\frac{r}{1\,\mathrm{km}}\right)^2\right). \quad (B2)$$

Denoting bulk density as ρ, their mass $M = \frac{4\pi}{3}\rho r^3$ can be written using Equation (B2) as

$$M = \frac{4\pi}{3}\frac{\rho}{\nu_r^{3/2}}10^{(13.94-H_r)\frac{3}{5}} = B\frac{\rho}{\nu_r^{3/2}}10^{-\frac{3H_r}{5}}, \quad (B3)$$

with $B = \frac{4\pi}{3}10^{13.96\frac{3}{5}}$ kg $= 9.685 \times 10^8$ kg and ρ given in kg.km^{-3} (1 g cm$^{-3} = 10^{12}$ kg.km^{-3}).

The computation of TNO mass from its absolute magnitude H_r thus strongly depends on the two unknowns ρ and ν_r. Conservatively assuming that ρ can vary from 0.5 g cm^{-3} to 2 g cm^{-3} and ν_r from 0.06 (as seen from the comets) to 0.24 (Arrokoth), we can formally have a variation by a factor of $\sim$30 in the mass of individual objects.

B.1. The Hot Belt

For a scenario of fixed values of the albedo and the bulk density, the mass of the hot belt is dominated by the few largest bodies (such as Makemake, Quaoar, Varda, or Varuna), but the predicted mass of these large bodies is badly overestimated if using nominal values of these quantities. With the nominal values of $\nu_r = 0.08$ (Lacerda et al. 2014), $\rho = 1$ g/cm^3 (Gladman et al. 2001; Fraser et al. 2014) and $H_r = -0.31$, one would find a mass for Makemake of $1.1\,10^{-2}M_\oplus$ when its actual mass is $5.2\,10^{-4}M_\oplus$ (Parker et al. 2018). The discrepancy decreases with increasing H_r but is still of a factor of 2 for Varuna at $H_r = 3.59$.

The simple solution of this issue is that Stansberry et al. (2008) showed a correlation between object size and geometric albedo, which Fraser et al. (2008) modeled as $\nu \propto r^\beta$. It is also likely that the density of a body increases with its size due to self-compression. In the mass-to-H_r relation, the important factor is $\rho\nu^{-3/2}$, which we then model as $\rho\nu^{-3/2} = A(M/1\,\mathrm{kg})^\gamma$. We select $\gamma = 0.77$ with resulting $A \sim 6.7 \times 10^{28}$ for ρ expressed in kg.km^{-3} to roughly match the known masses of Makemake, Quaoar ($M \simeq 1.4\,10^{21}$ kg, Vachier et al. 2012; Fraser et al. 2013), Varda ($M \simeq 2.45\,10^{20}$ kg, Souami et al. 2020), Varuna ($1.5\,10^{20}$ kg, Lacerda & Jewitt 2007; Lellouch et al. 2013), and (55637) 2002 UX25 ($1.2\,10^{20}$ kg, Brown 2013). We use this dependency for the large bodies until the $\rho\nu^{-3/2}$ factor reaches its nominal value for $\rho = 1$ g cm^{-3} and $\nu_r = 0.08$, which occurs at $M = 5.6\,10^{19}$ kg and $H_r = 4.82$. For smaller masses (larger H_r), we use the nominal values for ρ and ν.

Brightward of $H_r = 5.47$, we use the raw MPC absolute magnitude distribution. Between $H_r = 5.47$ and $H_r = 8.3$ we use the debiased H_r distributions shown in Figure 1. Faintward of this limit, we use the exponential cutoff from the cold belt (Equation (B4)) scaled up by a factor of 2.2 as in Figure 2. As expected, the mass is not concentrated at any given size. The total mass of the hot main classical belt is $0.012\,M_\oplus$.

B.2. The Cold Belt

For the cold population, all TNOs are small enough to be in the regime where albedos and densities are not correlated with their size. We use the nominal $\rho = 1000$ kg m^{-3} with more

reflective $\nu_r = 0.15$ (Fraser et al. 2014; Lacerda et al. 2014) estimated for cold objects. The debiased mass of the cold belt, brighter than $H_r = 8.3$ comes out as $0.0010 \, M_\oplus$.

For cold TNOs with $H_r > 8.3$, we use the exponential cutoff parameterization from Kavelaars et al. (2021),

$$N(<H_r) = 10^{\alpha(H_r - H_o)} \exp\left[-10^{-\beta(H_r - H_B)}\right], \quad (B4)$$

where N is the total population for TNOs with absolute magnitude less than H_r; $H_o = -2.6$ is a normalization factor; $\alpha = 0.4$ is the asymptotic logarithmic slope at large H_r; $\beta = 0.25$ is the strength of the exponential tapering; and $H_B = 8.1$ is the H_r value at which the exponential taper begins to dominate as one moves toward brighter magnitudes.[19] We caution that there is degeneracy in this parameterization, which allows individual parameters to have large variations as long as the others change in a correlated way, which results in the cumulative population curve being very similar. This yields a mass of $0.0011 \, M_\oplus$ for cold $H_r > 8.3$ TNOs, assuming $\alpha = 0.4$ continues.

Thus the total mass of the cold belt is $0.0021 \, M_\oplus$, for the assumed albedo and bulk density, or about one-sixth of our hot-belt mass estimate.

ORCID iDs

Jean-Marc Petit ⓘ https://orcid.org/0000-0003-0407-2266
Brett Gladman ⓘ https://orcid.org/0000-0002-0283-2260
J. J. Kavelaars ⓘ https://orcid.org/0000-0001-7032-5255
Michele T. Bannister ⓘ https://orcid.org/0000-0003-3257-4490
Mike Alexandersen ⓘ https://orcid.org/0000-0003-4143-8589
Kathryn Volk ⓘ https://orcid.org/0000-0001-8736-236X
Ying-Tung Chen ⓘ https://orcid.org/0000-0001-7244-6069

References

Abedin, A. Y., Kavelaars, J. J., Greenstreet, S., et al. 2021, AJ, 161, 195
Abod, C. P., Simon, J. B., Li, R., et al. 2019, ApJ, 883, 192
Adams, E. R., Gulbis, A. A. S., Elliot, J. L., et al. 2014, AJ, 148, 55
Alexandersen, M., Gladman, B., Kavelaars, J. J., et al. 2016, AJ, 152, 111
Ashton, E., Gladman, B., Kavelaars, J. J., et al. 2021, Icar, 356, 113793
Bannister, M. T., Gladman, B. J., Kavelaars, J. J., et al. 2018, ApJS, 236, 18
Benavidez, P. G., Campo Bagatin, A., Curry, J., Álvarez-Candal, Á., & Vincent, J.-B. 2022, MNRAS, 514, 4876
Bernstein, G. M., Trilling, D. E., Allen, R. L., et al. 2004, AJ, 128, 1364
Brown, M. E. 2008, in The Solar System Beyond Neptune, ed. M. A. Barucci et al. (Tuscon, AZ: Univ. of Arizona Press), 335
Brown, M. E. 2013, ApJL, 778, L34
Di Ruscio, A., Fienga, A., Durante, D., et al. 2020, A&A, 640, A7
Elliot, J. L., Kern, S. D., Clancy, K. B., et al. 2005, AJ, 129, 1117
Epanechnikov, V. A. 1969, Theory Probab. its Appl., 14, 153
Fraser, W. C., Batygin, K., Brown, M. E., & Bouchez, A. 2013, Icar, 222, 357
Fraser, W. C., Brown, M. E., Morbidelli, A., Parker, A., & Batygin, K. 2014, ApJ, 782, 100
Fraser, W. C., Kavelaars, J. J., Holman, M. J., et al. 2008, Icar, 195, 827
Gladman, B., Kavelaars, J. J., Petit, J.-M., et al. 2001, AJ, 122, 1051
Gladman, B., Lawler, S. M., Petit, J.-M., et al. 2012, AJ, 144, 23
Gladman, B., & Volk, K. 2021, ARA&A, 59, 203
Gomes, R. S., Morbidelli, A., & Levison, H. F. 2004, Icar, 170, 492
Greenstreet, S., Gladman, B., & McKinnon, W. B. 2015, Icar, 258, 267
Greenstreet, S., Gladman, B., McKinnon, W. B., Kavelaars, J. J., & Singer, K. N. 2019, ApJL, 872, L5
Grundy, W. M., Noll, K. S., Buie, M. W., et al. 2019, Icar, 334, 30
Hendler, N. P., & Malhotra, R. 2020, PSJ, 1, 75
Hofgartner, J. D., Buratti, B. J., Benecchi, S. D., et al. 2021, Icar, 356, 113723
Huang, Y., Gladman, B., & Volk, K. 2022a, ApJS, 259, 54
Huang, Y., Gladman, B., & Volk, K. 2022b, yCat, J/ApJS/259/54
Johansen, A., Oishi, J. S., Mac Low, M.-M., et al. 2007, Natur, 448, 1022
Kavelaars, J., Jones, L., Gladman, B., Parker, J. W., & Petit, J. 2008, in The Solar System Beyond Neptune, ed. M. A. Barucci et al. (Tuscon, AZ: Univ. of Arizona Press), 59
Kavelaars, J. J., Jones, R. L., Gladman, B. J., et al. 2009, AJ, 137, 4917
Kavelaars, J. J., Petit, J.-M., Gladman, B., et al. 2021, ApJL, 920, L28
Kenyon, S. J. 2002, PASP, 114, 265
Kenyon, S. J., Bromley, B. C., O'Brien, D. P., & Davis, D. R. 2008, in The Solar System Beyond Neptune, ed. M. A. Barucci et al. (Tuscon, AZ: Univ. of Arizona Press), 293
Klahr, H., & Schreiber, A. 2020, ApJ, 901, 54
Kobayashi, H., Tanaka, H., & Okuzumi, S. 2016, ApJ, 817, 105
Lacerda, P., Fornasier, S., Lellouch, E., et al. 2014, ApJL, 793, L2
Lacerda, P., & Jewitt, D. C. 2007, AJ, 133, 1393
Lellouch, E., Santos-Sanz, P., Lacerda, P., et al. 2013, A&A, 557, A60
Li, R., Youdin, A. N., & Simon, J. B. 2019, ApJ, 885, 69
Lissauer, J. J. 1993, ARA&A, 31, 129
McKinnon, W. B., Richardson, D. C., Marohnic, J. C., et al. 2020, Sci, 367, aay6620
Morbidelli, A., Bottke, W., Nesvorný, D., & Levison, H. 2009, Icar, 204, 558
Morbidelli, A., Levison, H. F., Tsiganis, K., & Gomes, R. 2005, Natur, 435, 462
Morbidelli, A., & Nesvorný, D. 2020, in The Trans-Neptunian Solar System, ed. D. Prialnik, M. A. Barucci, & L. Young (New York: Elsevier), 25
Morbidelli, A., Nesvorny, D., Bottke, W. F., & Marchi, S. 2021, Icar, 356, 114256
Nesvorný, D. 2018, ARA&A, 56, 137
Nesvorný, D., & Vokrouhlický, D. 2016, ApJ, 825, 94
Nesvorný, D., Vokrouhlický, D., Alexandersen, M., et al. 2020, AJ, 160, 46
Nesvorný, D., Vokrouhlický, D., & Roig, F. 2016, ApJL, 827, L35
Ormel, C. W. 2017, in Astrophysics and Space Science Library, Formation, Evolution, and Dynamics of Young Solar Systems, ed. M. Pessah & O. Gressel, Vol. 445 (New York: Springer), 197
Parker, A., Buie, M. W., Grundy, W., et al. 2018, AAS/DPS meeting, 50, 509.02
Parker, A. H., & Kavelaars, J. J. 2010, ApJL, 722, L204
Parzen, E. 1962, Ann. Math. Statist., 33, 1065
Pedregosa, F., Varoquaux, G., Gramfort, A., et al. 2011, JMLR, 12, 2825
Petit, J., Kavelaars, J. J., Gladman, B., & Loredo, T. 2008, in The Solar System Beyond Neptune, ed. M. A. Barucci et al. (Tuscon, AZ: Univ. of Arizona Press), 71
Petit, J., & Mousis, O. 2004, Icar, 168, 409
Petit, J.-M., Kavelaars, J. J., Gladman, B. J., et al. 2011, AJ, 142, 131
Petit, J.-M., Kavelaars, J. J., Gladman, B. J., et al. 2017, AJ, 153, 236
Pike, R. E., Fraser, W. C., Schwamb, M. E., et al. 2017, AJ, 154, 101
Pitjeva, E. V., & Pitjev, N. P. 2018, CeMDA, 130, 57
Rosenblatt, M. 1956, Ann. Math. Statist., 27, 832
Schäfer, U., Yang, C.-C., & Johansen, A. 2017, A&A, 597, A69
Schaller, E. L., & Brown, M. E. 2007, ApJL, 659, L61
Schlichting, H. E., & Sari, R. 2011, ApJ, 728, 68
Schwamb, M. E., Fraser, W. C., Bannister, M. T., et al. 2019, ApJS, 243, 12
Shannon, A., Wu, Y., & Lithwick, Y. 2016, ApJ, 818, 175
Sheppard, S. S., Udalski, A., Trujillo, C., et al. 2011, AJ, 142, 98
Singer, K. N., McKinnon, W. B., Gladman, B., et al. 2019, Sci, 363, 955
Souami, D., Braga-Ribas, F., Sicardy, B., et al. 2020, A&A, 643, A125
Spencer, J. R., Stern, S. A., Moore, J. M., et al. 2020, Sci, 367, aay3999
Stansberry, J., Grundy, W., Brown, M., et al. 2008, in The Solar System Beyond Neptune, ed. M. A. Barucci et al. (Tuscon, AZ: Univ. of Arizona Press), 161
Tancredi, G., & Favre, S. 2008, Icar, 195, 851
Tegler, S. C., Romanishin, W., & Consolmagno, G. J. 2003, ApJL, 599, L49
Vachier, F., Berthier, J., & Marchis, F. 2012, A&A, 543, A68
Van Laerhoven, C., Gladman, B., Volk, K., et al. 2019, AJ, 158, 49
Vilenius, E., Kiss, C., Müller, T., et al. 2014, A&A, 564, A35
Weryk, R. J., Lilly, E., Chastel, S., et al. 2016, arXiv:1607.04895
Willmer, C. N. A. 2008, http://mips.as.arizona.edu/~cnaw/sun.html

---

[19] Note that the numbers in Table 1 are obtained from debiasing of OSSOS data, not from this formula.